CARBON letters

Original Articles
Carbon Letters Vol. 22, 48-59 (2017)

Synthesis and characterization of carbon doped TiO_2 photocatalysts supported on stainless steel mesh by sol-gel method

JO. Tijani[1,2,♠], OO. Fatoba[1], TC. Totito[1], WD. Roos[3] and LF. Petrik[1]

[1]Environmental and Nano Sciences Research Group, Department of Chemistry, University of the Western Cape, Cape Town 7535, Republic of South Africa
[2]Department of Chemistry, Federal University of Technology, Minna Private Mail Bag 65, Nigeria
[3]Department of Physics, University of the Free State, Bloemfontein 9300, Republic of South Africa.

Article Info
Received 6 October 2016
Accepted 11 February 2017

♠Corresponding Author
E-mail: jimohtijani@futminna.edu.ng
Tel: +234-8057344464

Open Access
DOI: http://dx.doi.org/10.5714/CL.2017.22.048

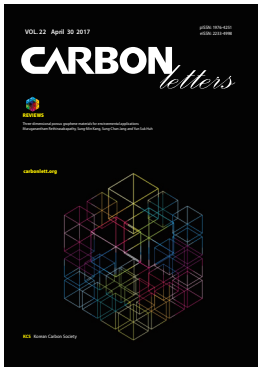

http://carbonlett.org

pISSN: 1976-4251
eISSN: 2233-4998

Abstract

This study synthesized pure anatase carbon doped TiO_2 photocatalysts supported on a stainless steel mesh using a sol-gel solution of 8% polyacrylonitrile (PAN)/dimethylformamide (DMF)/$TiCl_4$. The influence of the pyrolysis temperature and holding time on the morphological characteristics, particle sizes and surface area of the prepared catalyst was investigated. The prepared catalysts were characterized by several analytical methods: high resolution scanning electron microscopy (HRSEM), energy dispersive spectroscopy (EDS), X-ray diffraction (XRD), Brunauer-Emmett-Teller (BET), and X-ray photoelectron spectroscopy (XPS). The XRD patterns showed that the supported TiO_2 nanocrystals are typically anatase, polycrystalline and body-centered tetragonal in structure. The EDS and XPS results complemented one another and confirmed the presence of carbon species in or on the TiO_2 layer, and the XPS data suggested the substitution of titanium in TiO_2 by carbon. Instead of using calcination, PAN pyrolysis was used to control the carbon content, and the mesoporosity was tailored by the applied temperature. The supported TiO_2 nanocrystals prepared by pyrolysis at 300, 350, and 400ºC for 3 h on a stainless steel mesh were actual supported carbon doped TiO_2 nanocrystals. Thus, PAN/DMF/$TiCl_4$ offers a facile, robust sol-gel related route for preparing supported carbon doped TiO_2 nanocomposites.

Key words: TiO_2 photocatalyst, sol-gel method, stainless steel mesh, carbon doping

1. Introduction

Semiconductor oxides such as TiO_2, ZnO, SnO_2, GaP, CdS, ZnO, and ZnS have been widely used as catalysts in the abatement of water pollution, especially in the decomposition of emerging organic contaminants to less toxic and harmless inorganic compounds [1,2]. Of all the aforementioned semiconductor metal-oxides, TiO_2 based photocatalysts have received the greatest scientific interest in fundamental research in the last decade evident by the large number of publications in the field of heterogeneous photocatalysis. TiO_2 based photocatalysts are greatly preferred over other metal-oxide catalysts due to their excellent photophysical and photocatalytic properties, photo-stability and non-toxicity, among others [3,4]. Titanium (IV) oxide, often referred to as titania, titanium white, titanic anhydride, or titanic acid anhydride occurs naturally as an oxide of titanium. It exists in four different polymorphs namely rutile, anatase, brookite and titanium (IV) oxide B. These crystal structures differ appreciably from one another through the bond angle distortion of the octahedral chains [4]. The application of TiO_2 as a photocatalyst dated back to 1972 when Fujishima and Honda employed a photo-electrochemical cell consisting of a rutile titania anode and inert cathode to split water into hydrogen and oxygen. This achievement served as a turning point in the history of heterogeneous photocatalysis. Ever since then, scientists across the globe have conducted far reaching research trying to understand the fundamental mechanism of TiO_2

photocatalysts [5]. It should be pointed out that the application of powdered TiO_2 photocatalysts in wastewater treatment could be more advantageous than using supported TiO_2 catalysts. This is because powdered TiO_2 photocatalysts have a high surface area which enables adequate surface coverage of the particles on the contaminated liquid and intimate contact with the pollutants. Despite easy miscibility with the pollutants, use of powdered TiO_2 is often associated with certain challenges such as post recovery and separation of the nanoparticles after the purification process [6]. Most importantly, light has difficulty penetrating a solution containing suspended titania nanoparticles thus limiting its industrial applications [6]. Conversely, in the case of a supported TiO_2 photocatalyst with a restricted surface area compared to powdered TiO_2, post filtration and recovery of the nanoparticles after treatment are not necessary. Not only that, efficient light penetration in a photochemical reactor is guaranteed [7].

Several methods of synthesizing supported and unsupported TiO_2 photocatalysts have been reported in the literature namely photodeposition process, physical vapor deposition, electron beam evaporation, chemical vapor deposition, boil deposition, solvo-thermal, thermal evaporation, dip coating, electrochemical, wet impregnation, sol-gel process, hydrothermal, and pulsed laser deposition method among others [6,8]. Of all these methods, the sol-gel technique appears to be the most promising and simple to use due to the production of nanoparticles with good homogeneity in terms of the morphology, surface area, phase structure and average crystallite size [9]. Other advantages of sol-gel methods are as follows: they can be used on different substrate materials; they are easily performed with ordinary laboratory equipment, and they can achieve a uniform coating of high contact areas and complex shapes [10]. In view of the inherent shortcomings associated with the powder TiO_2 nanoparticles, several attempts have been made to immobilize TiO_2 nanoparticles onto different categories of supports such as glasses, ceramics, polymers, clay minerals, carbon nanotubes, activated carbon, cellulose fibres, carbon fibres, and stainless steel meshes among others [7,11,12]. Among the listed support materials often used to immobilize TiO_2 photocatalysts, stainless steel meshes possess exceptional features compared to other supports, which include maintenance of structural integrity under high heat treatment (during calcination of TiO_2). Other materials such as quartz glass deform and melt depending on the glass transition temperature. Apart from the aforementioned, stainless steel meshes can be used in electrochemical processes while quartz and ceramics cannot be used due to their dielectric properties. Moreover, stainless steel meshes can be readily used in complex shapes and have outstanding mechanical properties [7,8].

Previous studies have shown that TiO_2 nanoparticles can be easily prepared and supported on a substrate such as a stainless steel mesh. For instance, Fernández et al. [13] prepared a stainless steel mesh supported TiO_2 photocatalyst using a sol-gel method involving a mixture of titanium isopropoxide and propano followed by a dip-coating procedure and found that a pure anatase phase was obtained for the TiO_2 photocatalyst calcined at 973 K irrespective of the holding time (4 and 8 h). However, the authors did not use a polymer precursor, and the proper optimization of the calcination temperature on the surface area as well as the crystalline nature and morphology of the nanoparticles was not investigated. Li et al. [14] synthesized supported TiO_2 nanoparticles using the metal organic chemical vapor deposition method involving the introduction of titanium isopropoxide vapor and the subsequent deposition onto a stainless steel mesh placed inside a horizontal quartz reactor chamber containing argon as an inert gas. The influence of the deposition temperature from 250 to 750ºC was investigated, and it was found that anatase phase formation and particle size were temperature dependent. The authors did not investigate the influence of the holding time on the particle size; moreover, no polymer precursor was used during the synthesis. Zhang et al. [15] used a sol-gel solution containing titanium isobutyl oxide, ethanol and polyethylene glycol to prepare a TiO_2 film photocatalyst supported on stainless steel calcined at 400ºC. The authors found that polyethylene glycol acted as a stabilizer and was responsible for the high mesoporosity of the TiO_2 film photocatalyst with a pore diameter of approximately 15 nm. However, the authors did not investigate the influence of the calcination temperature and the holding time on the particle size. Likewise, the role of carbon released by polyethylene glycol during calcination was not mentioned. El-Kalliny et al. [7] used the sol-gel dip coating and electrophoretic deposition method to immobilize TiO_2 nanoparticles on stainless steel woven meshes. The authors showed that the electrophoretic deposition technique produced better homogeneous and strongly adhered TiO_2 nanoparticles supported on stainless steel woven meshes compared to the dip coating method with a calcination temperature of 300ºC. On the other hand, the authors did not examine the effect of the calcination temperature and the holding time on the crystalline nature and morphology of the TiO_2 nanoparticles. Habibi et al. [16] prepared alumina supported TiO_2 nanoparticles using the sol-gel method and found the optimal conditions for the calcination temperature (550ºC), refluxing temperature (66ºC) and calcination time (2 h). Wang et al. [17] synthesized Cr-doped TiO_2 nanoparticles supported on a natural zeolite via hydrothermal treatment and found that the optimal calcination temperature was 400ºC. Omri et al. [18] synthesized TiO_2 nanoparticles supported on activated carbon made from almond shells using a combination of the hydrothermal and sol-gel method. The authors showed that both crystal phases observed in both the TiO_2 nanoparticles and activated carbon supported TiO_2 nanoparticles were anatase and rutile in nature with the anatase content having a higher percentage. It should be mentioned that a TiO_2 photocatalyst supported on stainless steel using the electrophoretic deposition and sol-gel method involving titanium tetraisopropoxide as a titanium precursor has been separately reported [7,10].

However, a review of the literature indicates that no report exists on the synthesis of carbon doped TiO_2 photocatalysts supported on a stainless steel mesh in which a polymer precursor such as polyacrylonitrile (PAN) simultaneously serves as a carbon dopant and stabilizing agent. Similarly, limited information exists on the influence of the pyrolysis temperature and holding time on the control of crystallite sizes. Herein, we report for the first time a novel, simple sol-gel method containing 8% PAN, n, n-dimethylformamide and titanium tetrachloride to synthesize a carbon doped TiO_2 photocatalyst supported on a stainless steel mesh, for which the influence of the pyrolysis temperature and the holding time on the morphology and sizes of the particles was investigated

2. Experimental

2.1. Materials

$TiCl_4$ (99%), PAN powder (99%), and pure dimethylformamide (DMF) (99.5%) were obtained from Sigma Aldrich (USA). The chemicals were of analytical grade and used without any further purification.

2.1.1. Synthesis of supported carbon doped TiO_2 nanocrystals

A TiO_2 photocatalyst supported on a stainless steel mesh was synthesized by the sol-gel technique as follows. First, 8 g of powdered PAN were added to 92 g of DMF making up 100 g of PAN and DMF. PAN with a high strength, thermal resistance, and elastic modulus and a low density served as the carbon precursor while DMF, an aprotic solvent, was used for the dissolution of PAN which aids in the reduction of the thermal effect from the cyclization process. The mixture in a bottle was sealed and then stirred on a magnetic stirrer at room temperature (25ºC) for 12 h. After 12 h of stirring, a slightly transparent (8%) PAN/DMF viscous solution was obtained. From the solution, 50 mL of the mixture were placed in a separate bottle followed by the slow, drop wise addition of 6 mL of 0.09 M $TiCl_4$ at 25ºC using a magnetic stirrer for continuous stirring at 150 rpm. This step was done in a ventilated fume hood. During the addition of the 6 mL of 0.09 M $TiCl_4$, the transparent solution rapidly became brownish yellow in color. The addition of 6 mL of 0.09 M $TiCl_4$ was accompanied by the release of white fumes of hydrochloric acid, and the stirring was continued for 15 min. until the white fumes disappeared. Prior to the addition of $TiCl_4$, the temperature of the sol was 25ºC, and after the addition of the titanium precursor, the temperature increased to 41ºC. The formed viscous solution was continually stirred until the white fumes disappeared.

2.1.2. Coating of the stainless steel mesh with 8% transparent PAN/DMF/$TiCl_4$ sol gel solution

Prior to the manual coating, a 4×4 cm stainless steel mesh was rinsed with acetone, ethanol and water and then dried in an oven at 90°C for 5 min. The reason for cleaning the mesh with acetone was to remove any organic and inorganic contaminants. The cleaned stainless steel mesh was weighed and coated manually with the prepared sol-gel formulation. The sol-gel solution was coated on a 4×4 cm stainless steel mesh using the dip-coating method with a drawing speed of 5.0 cm/min. This procedure was repeated three times, and afterwards, the coated mesh was oven dried at 90°C for 5 min followed by pyrolysis in a N_2 atmosphere at 300, 350 or 400°C in a Labfurn tube furnace. A heating rate of 50ºC/min. and a holding time of 1 to 4 h were used. The procedure also included a flow of nitrogen gas through the inner tube at 20 mL/min to create an inert environment and to prevent side reactions such as hydrolysis. The various synthesized supported TiO_2 nanocrystals prepared at 300ºC with a 1–4 h holding time were denoted as JT1, JT2, JT3, and JT4. Similarly, calcined stainless steel mesh supported TiO_2 nanocrystals at 350 and 400ºC with a 1–4 h holding time were denoted as JT5, JT6, JT7, JT8, JT9, JT10, JT11, and JT12. The thicknesses of the various supported TiO_2 photocatalysts were approximately 250 nm.

2.2. Characterization techniques

The crystal phases as well as the crystallite size of the synthesized TiO_2 photocatalyst, supported on a stainless steel mesh, were determined by powder X-ray diffraction (XRD) analysis performed on a Bruker AXS D8 Advance (USA) with Cu-Kα radiation. The formed crystals were removed from the stainless steel mesh by physical abrasion and subjected to characterization. A portion of the crystals were sprinkled on a de-greased glass slide, and diffractograms were recorded between diffraction angles of 20º and 80º. The morphology of the synthesized materials was examined using a Zeiss Auriga HRSEM (USA). A crystal sample (0.05 mg) was sprinkled onto carbon adhesive tape and sputter coated with Au-Pd using a Quorum T15OT for 5 min prior to the analysis. The microscope was operated with electron high tension at 5 kV for imaging. High resolution scanning electron microscopy (HRSEM) equipped with energy dispersive spectroscopy (EDS) was further used to determine the elemental composition of the synthesized catalysts. The particle size and distribution pattern were analyzed by a Zeiss Auriga High resolution transmission electron microscope. Approximately, 0.02 g of the synthesized products were suspended in 10 mL of methanol and thereafter subjected to ultra-sonication until complete dispersion was achieved. One or two drops of the slurry were dropped onto a holey carbon grid with the aid of a micropipette and subsequently dried by exposure to a photo light. For Brunauer-Emmett-Teller method (BET) N_2 adsorption, about 100 mg of a dry powder sample in a sample tube were first degassed at 90ºC for 4 h to remove any residual water and other volatile components that were likely to block the pores. The BET surface area and average pore volume distributions were obtained from the plot of the volume adsorbed (cm^3/g STP) versus relative pressure. The N_2 adsorption-desorption isotherms were collected at –196ºC using a Micromeritics ASAP 2020 accelerated surface area and porosimetry analyser. A XPS PHI 5400 equipped with hemispherical sector analyser operated using non-monochromated Al K_α X-rays with an energy of 1486.6 eV at 300 W and 15 kV was used to examine the surface composition of the material. The energy scale was calibrated using Au $4f_{7/2}$ at 83.95 eV, and the linearity of the scan was adjusted to measure Cu $2p_{3/2}$ at a position of 932.63 eV. Surveys were scanned (2.5 eV/s) with a pass energy of 178 eV, and detail spectra were collected with a pass energy of 44 eV and a scan rate of 0.625 eV/s. The photoelectron take-off angle for all measurements was 45º. All spectra obtained were energy corrected using the aliphatic adventitious hydrocarbon C (1s) peak at 284.8 eV. The XPSPeak 4.1 software (http://xpspeak.software.informer.com/4.1/) was used for data analysis and fits. Thermal gravimetric and differential scanning calorimetry (TGA-DSC) analysis of the dried synthesized catalyst was performed in a Perkin Elmer STA 4000 (USA). A 25 mg sample was placed in a sample pan, and the thermal behavior of the materials was analyzed from 30 to 800°C with a heating rate of 10°C/min. Over this temperature range, nitrogen, operating at a flow rate of 20 mL/min, was used as a purging gas.

3. Results and Discussion

3.1. Characterization of the supported carbon doped TiO_2 photocatalysts

The results of the HRSEM characterization of the supported carbon doped TiO_2 nanocrystals synthesized by the sol-gel method are presented below.

3.1.1. The HRSEM results of the synthesized supported carbon doped TiO_2 nanocrystals

Figs. 1-3 shows the HRSEM micrographs of the supported TiO_2 catalysts ramped (50ºC/min) from 20 to 300ºC, 350 or 400ºC, respectively, in a N_2 atmosphere with a holding time of 1 to 4 h

Fig. 1 shows the HRSEM micrographs of the synthesized supported TiO_2 catalysts pyrolyzed at 300ºC between 1 to 4 h. The HRSEM image of JT1 (Fig. 1a) shows the formation of irregular and scattered nanocrystals. This result suggests pyrolysis of the PAN because it is not stable above 200ºC followed by the initiation of crystallization of the $TiCl_4$ precursor into TiO_2 under the set conditions. It is important to mention that the in situ crystallization process commenced immediately when $TiCl_4$ was added. During the addition of the 6 mL of 0.09 M $TiCl_4$, there was a sudden change in color of the solution from a transparent to a highly viscous brownish yellow color. The sudden change of color under excessive air in a ventilated fume hood indicated an oxidation reaction because $TiCl_4$ is known to oxidize to TiO_2 upon contact with air and subsequently releases HCl as shown in Eq. 1.

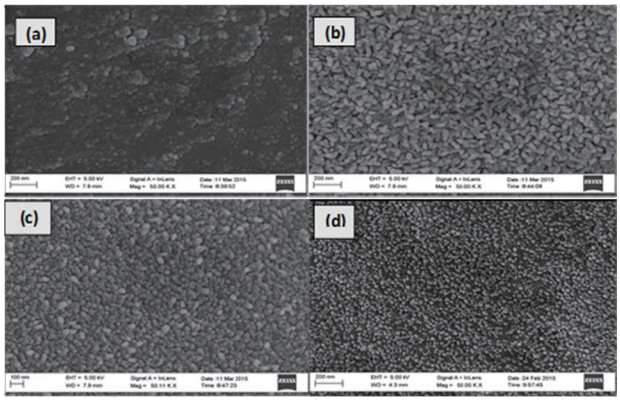

Fig. 1. High resolution scanning electron microscopy image of a catalyst prepared at 300ºC: (a) JT1 (1 h), (b) JT2 (2 h), (c) JT3 (3 h), (d) JT4 (4 h) at a constant heating rate of 50ºC/min

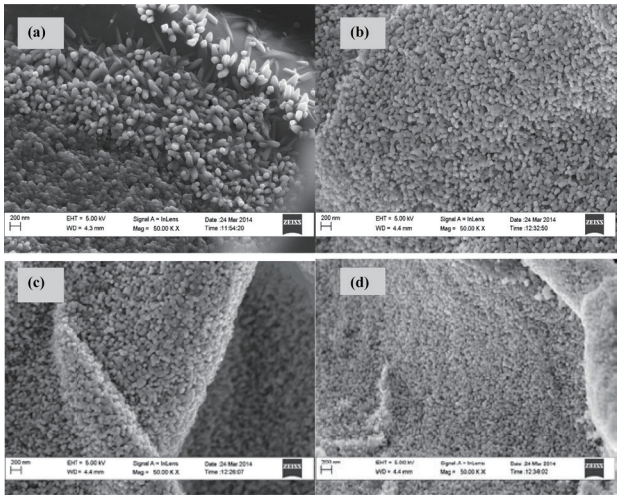

Fig. 2. High resolution scanning electron microscopy image of a catalyst prepared at 350ºC: (a) JT5 (1 h), (b) JT6 (2 h), (c) JT7 (3 h), (d) JT8 (4 h) at a constant heating rate of 50ºC/min.

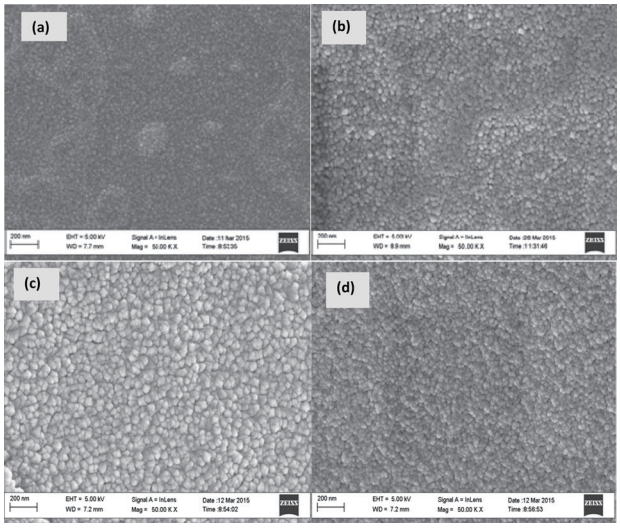

Fig. 3. High resolution scanning electron microscopy image of a catalyst prepared at 400ºC: (a) JT9 (1 h), (b) JT10 (2 h), (c) JT11 (3 h), (d) JT12 (4 h) at a constant heating rate of 50ºC/min.

$$4 \sim C_3H_3N + 4C_3H_7O + TiCl_4 \xrightarrow{excess\ air\ (O_2)} 4C_3H_3N - CO - NC_2H_6 + TiO_2 + 4HCl \uparrow \quad (1)$$

In addition, there was a substitution of the oxygen atoms in the DMF by chlorine atoms from $TiCl_4$ and a subsequent replacement of the chlorine by oxygen resulting in the formation of the TiO_2 nanoparticles. This was possibly responsible for the release of the white hydrochloric acid fumes accompanying the temperature increase implying that the reaction was purely exothermic. Prior to the addition of $TiCl_4$, the temperature of the sol was 20ºC, and after the addition of the titanium precursor, the temperature rose to 41ºC. This indicates that the oxygen in the DMF or free oxygen in the ventilated fume hood displaced the chlorine in the $TiCl_4$ to yield TiO_2. After the manual coating of the sol-gel onto the stainless steel mesh, the coated mesh was air dried at room temperature in a ventilated fume cupboard for 10–15 min. The brownish color later turned to black. The color changes may be due to exposure to air. According to Rahaman et al. [19], the phenomenon and mechanism of the appearance or disappearance of color is complex and not fully understood. Nevertheless, the authors ascribed the black coloration of the PAN on expo-

sure to air to the formation of a ladder ring structure due to conversion of the C≡N to C=N. The second reaction was the thermal pyrolysis of the PAN into carbon during the heating period inside the programmable tube furnace and the complete formation of TiO_2 nanocrystals shown in Eq. 2.

$$4C_3H_3B - CO - NC_2H_6 + TiO_2 \xrightarrow{heat\ (300\text{-}400^oC)\ in\ N_2\ atmosphere} 4C_2H_2O + 4C_2H_6N + 4HCN + 4C + TiO_2 \quad (2)$$

For the 2 h holding time of JT2 (Fig. 1b), there was a sudden color change from brown to black upon visual inspection, possibly due to pyrolysis and carbonization of the PAN polymer or perhaps due to the decrease in the nitrile bond strength [20]. The 2 h heating period resulted in the formation of uniformly distributed and densely agglomerated TiO_2 nanocrystals. The shape and sizes of the TiO_2 crystals were not uniform and remained unchanged even at a 3 h holding time shown in the HRSEM image of JT3. During the 3 h holding time, PAN is undergoing pyrolysis and carbonization leading to the disappearance of the PAN peaks (see XRD results shown in Figs. 5-7). Subsequently, homogeneous, and evenly distributed TiO_2 nanocrystals were observed (JT3). At 4 h (JT4) (Fig. 1d), some nanocrystals fell off the stainless steel mesh which could be due to the prolonged holding time, which resulted in a complete loss of the carbonaceous species causing a weak interaction between the stainless steel mesh and the TiO_2 nanocrystals. It is important to stress that PAN and its pyrolysis or decomposition products act as an adhesive that causes the TiO_2 crystals to adhere together and onto the stainless steel mesh. However, when the holding time is too long or the temperature is too high, all the PAN and carbon burn away, and the TiO_2 crystals fall off the mesh. Despite their low adhesion, the imaged crystals were still homogeneous and spherical, but less agglomerated and loosely bound to each other.

In Fig. 2a, at a 1 h holding time at 350ºC (JT5), the formation of both TiO_2 nano rods and densely packed aggregated TiO_2 nanocrystals that adhered to the stainless steel mesh was observed. At 2 h (Fig. 2b, sample JT6), the TiO_2 nano rods disappeared and thereafter transformed completely to fully grown, closely packed, identical TiO_2 nanocrystals. It was observed that there were no clear differences in the HRSEM micrographs of Fig. 2b-d despite the increase in the holding time. All the samples had a uniform particle size, and the longer holding times did not alter the spheroidal spherical crystal morphology. Again, uniformly monodispersed, spherical and agglomerated TiO_2 nanocrystals were evident. Moreover, during the photocatalytic activity, there was loss of crystals off the mesh for the 4 h holding time. This was plausibly due to structural changes of the polymer to carbon and complete conversion of the titanium precursor to the oxide form which produced TiO_2 nanocrystals of identical sizes in the inert environment. Abdo et al. [21] had previously reported that the carbonization process of PAN in air, at temperatures between 600 and 1000ºC for 1 h at a heating rate of 4.5ºC/min, was associated with the release of more than 90% carbon and other volatile compounds such as HCN, H_2O, and N_2. Furthermore, a similar trend was observed at 400ºC irrespective of the holding time (Fig. 3). The appearance of agglomerated spherical TiO_2 nanocrystals which showed some degree of homogeneity can be ascribed to the extensive decomposition of the PAN as the holding time increased. Although the shape and size of the nanocrystals were not uniform, it was observed that the pyrolysis temperature (300, 350, and 400ºC) and the holding time (3 h) had an effect on the size and shape of the TiO_2 nanocrystals and on their adhesion. Ba-Abbad et al. [22] reported that temperature had a profound effect on the particle size, shape and catalytic activity of TiO_2 nanoparticles synthesized with the sol-gel method made up of titanium tetra isopropoxide, ethanol and water.

Generally, irrespective of the temperature, it was observed that at a longer holding time, specifically 4 h, all the PAN decomposed, and the TiO_2 crystals fell off the mesh. Based on this, the 3 h holding time was selected as the optimum holding time required to achieve uniform growth of the crystals for the three temperatures. For a holding time longer than 3 h, there was a noticeable loss of the binding force between the stainless steel mesh and the TiO_2 nanocrystals, which was ascribed to the extensive decomposition of the PAN. From the results presented (Figs. 1-3), it is apparent that the supported TiO_2 nanocrystals are of different shapes and sizes, which occurred due to the heating conditions applied. In summary, two important reactions occurred during the synthesis of the supported carbon doped TiO_2 nanocrystals. The first reaction was the oxidation of $TiCl_4$ to TiO_2 through the in situ crystallization mechanism shown in Eq. 1. This took place prior to pyrolysis in the furnace. The growth of the crystals commenced immediately after the $TiCl_4$ precursor was added to the PAN/DMF solution in a ventilated fume hood. The second reaction was the thermal combustion of the PAN in the furnace transforming it to different carbonaceous species (Eq. 2). This is also supported by the X-ray photoelectron spectroscopy (XPS) results shown in Fig. 4. It should be noted that the TiO_2 nanocrystals were strongly adhered onto the stainless steel support by the carbonaceous species resulting from the pyrolysis of the PAN.

3.1.2. EDS result of the supported TiO_2 nanocrystals

EDS analysis was done to investigate the elemental composition of the supported carbon doped TiO_2 nanocrystals pyrolyzed at 300, 350, and 400ºC and at holding times of 1–4 h. The samples were coated with Pd and Au to prevent charging during the scanning electron microscopy (SEM) analyses, which can distort the images. The atomic% of each element, as revealed by EDS, in samples JT1 through JT12 is presented in Table 1.

According to Table 1, the supported TiO_2 nanocrystals contained the following elements: Ti, O, C, Cr, Fe, Ni, and Cl at different proportions irrespective of the temperature and holding time. The values listed in Table 1 represent the average of three spots scanned indicating that the values were representative. The atomic percentage of Ti and O in each sample varied with the pyrolyzed temperature and holding time. Even though EDS analysis is not a quantitative measure of the concentration of each element on the surface, it can provide information on the type of elements in bulk of a sample. As seen in Table 1, the ratio of Ti to O at 300ºC was 1:1 and changed to 1:2 when the temperature was increased to 350 and 400ºC at a longer holding time of 3 h. The observed ratio of 1:1 suggests a dilution by PAN at a lower temperature (300ºC), which corroborates

Table 1. Energy dispersive spectroscopy spectrum of the supported TiO_2 nanocrystals in atomic percentage for different pyrolyzed temperatures and holding times

Sample name	Elemental composition (atomic%)						
	Ti	O	C	Cr	Fe	Ni	Cl
JT1	25.21	31.35	19.73	7.15	8.12	3.92	3.52
JT2 Ti:O ratio (1:1)	27.78	32.11	17.98	5.74	7.21	3.54	5.64
JT3	37.14	31.56	14.17	4.04	7.64	2.87	2.58
JT4	39.45	29.76	10.54	7.29	8.23	2.52	2.21
JT5	43.56	30.37	10.34	4.41	7.45	2.53	1.34
JT6 Ti:O ratio (1:2)	44.88	28.75	8.86	5.45	7.50	3.45	1.11
JT7	45.13	26.94	8.23	4.49	7.92	3.40	3.89
JT8	43.55	30.30	7.81	5.33	6.97	2.88	3.16
JT9	45.57	27.50	5.32	6.28	8.19	4.12	3.02
JT10 Ti:O ratio (1:2)	45.38	32.80	5.25	5.52	6.02	2.61	2.42
JT11	54.89	22.64	4.41	6.19	6.80	2.09	2.98
JT12	68.04	10.32	2.31	6.88	7.56	1.38	3.51

the XRD results shown in Fig. 5, in which the graphitic carbon peaks were prominent. As the temperature increased, the Ti:O ratio increased, which was evidence of the thermal pyrolysis and decomposition of the PAN. The slow oxidation of $TiCl_4$ to TiO_2 during pyrolysis may be due to the changing ratio of Ti to O. Along the same line, as seen in Table 1, the weight percentage of the carbon content decreased from 19.73 observed at 300ºC for 1 h to 2.31 at 400ºC for a 4 h holding time. There was a clear decrease in carbon content as the temperatures (300–400ºC) and the holding times (1–4 h) increased, which suggests the partial or extensive decomposition of the PAN. The decrease in the carbon content as evident in the EDS results corroborates the XRD results shown in Figs. 5-7. This further confirmed the direct carbon doping and the adhesive role of the pyrolysis products.

Because the samples were not coated with carbon, the probable sources of carbon in the samples could be traced to the PAN or the holey grids. However, XPS analysis carried out on the samples further confirmed that the amount of carbon in the catalysts did not come from the holey carbon grids but rather from the PAN precursor (Fig. 8) [23]. In addition, Abdo et al. [21] previously reported that the carbonization of PAN is associated with the release of more than 90% carbon and other volatile compounds such as HCN, H_2O, and N_2. The presence of carbon in the EDS results suggests that the PAN decomposed to carbon that was present in the supported TiO_2 nanocrystals, which is in agreement with the XPS results shown in Fig. 8. Furthermore, the EDS spectra also showed the presence of Fe, Cr, and Ni, which originated from the stainless steel mesh due to the thermal effect [24-25]. The presence of chlorine could be linked to the titanium precursor used ($TiCl_4$) The thermal treatment caused the diffusion of Fe, Cr, and Ni from the stainless steel mesh into the TiO_2 layer due to the lowered driving force of diffusion in the crystal energy [26]. These elements (Fe, Cr, and Ni) have been reported to also act as dopants for titania [27]. A similar phenomenon was reported by Fernández et al. [13] during the synthesis of TiO_2 photocatalysts on rigid supports such as stainless steel. The authors synthesized TiO_2 nanoparticles by dissolving 1 g of commercial TiO_2 (Degussa, Germany) in 100 mL acetone and subsequently used an electrophoretic method to deposit the TiO_2 particles onto the stainless steel. The supported TiO_2 nanoparticles were calcined in a N_2 atmosphere at 700ºC for 4 and 8 h, respectively. They found that Fe, Si and Cr in the stainless steel diffused into the titania lattice structure during the thermal treatment.

.

3.1.3. Thermal Gravimetric Analysis/ Differential Scanning Calorimetry (TGA-DSC) analysis

TGA-DSC plots show the physico-chemical structural changes such as loss of moisture and other volatile organic compounds present in the sample. The results of the heat-profile of raw 8% PAN/DMF/TiCl4 are presented in Fig. 4. This was done to determine the temperature at which PAN starts to decompose.

Fig. 4 shows an increase in weight loss as the temperature was increased. A substantial weight loss was observed before 350ºC after which the TGA curve remained nearly flat until 800ºC. There are three prominent temperature regions where weight loss can be seen in the TGA curve. The first residual weight loss of ~10.2% was observed from 30 to 150°C. This is attributed to the dehydration of the adsorbed DMF embedded within the PAN. The second weight loss of ~50.8% was observed between 172 and 330°C and can be ascribed to the pyrolysis of the unhydrolyzed PAN, which is accompanied by a peak (exotherm) at 172ºC in the DSC plot. This is because PAN is not stable above 200ºC [28]. The further weight loss of ~19.51% before 350ºC could be due to the decomposition of other residual intermediate carbonaceous species in the PAN as products of the pyrolysis before complete carbonization. The DSC curve shows an endothermic peak localised at 137.7°C and two sharp exothermic peaks at 172 and 300ºC. The slight endothermic peak localised in the DSC curve at 137.7ºC could be due to volatilization of the

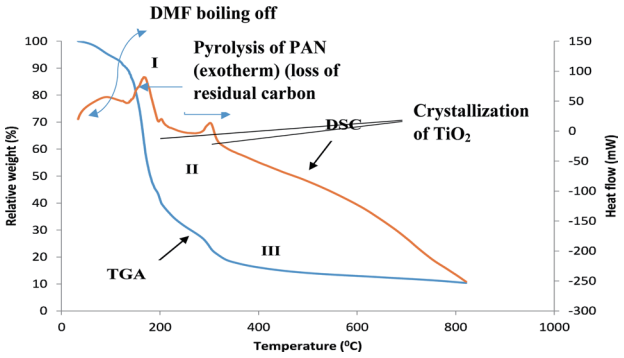

Fig. 4. Thermal Gravimetric and Differential Scanning Calorimetry (TGA-DSC) curves of the wet sol-gel solution (8% PAN/DMF/$TiCl_4$) measured at a heating rate of 10°C/min in a nitrogen atmosphere with a purging flow rate of 20 mL/min. PAN, polyacrylonitrile; DMF; dimethylformamide

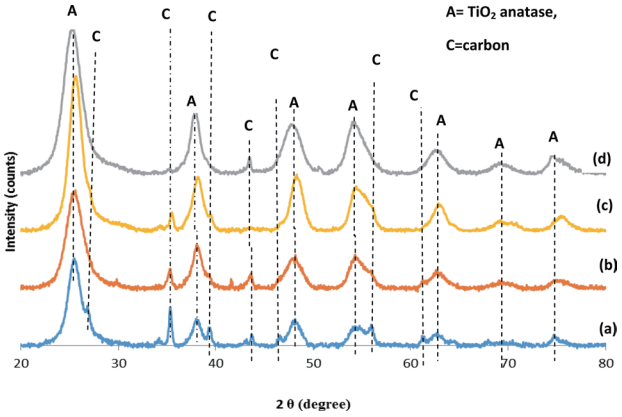

Fig. 5. X-ray diffraction pattern of the catalysts: (a) JT1 (300°C for 1 h), (b) JT2 (300°C for 2 h), (c) JT3 (300°C for 3 h), and (d) JT4 (300°C for 4 h) at a constant heating rate of 50°C/min. A, anatase; C, carbon

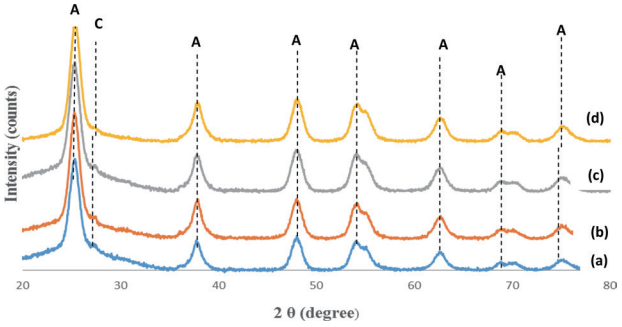

Fig. 6. X-ray diffraction pattern of the catalysts: (a) JT5 (350°C for 1 h), (b) JT6 (350°C for 2 h), (c) JT7 (350°C for 3 h), and (d) JT8 (350°C for 4 h) at a constant heating rate of 50°C/min. A, anatase; C, carbon.

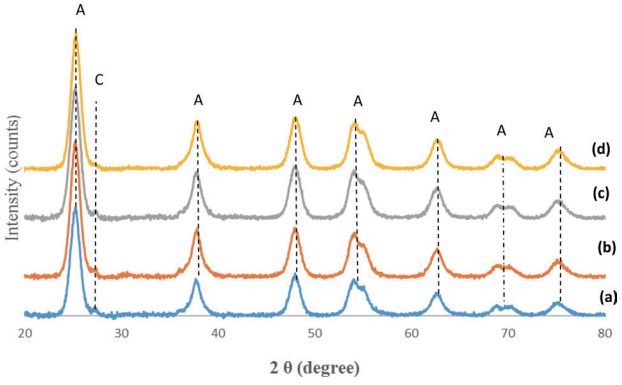

Fig. 7. X-ray diffraction pattern of the catalysts: (a) JT9 (400°C for 1 h), (b) JT10 (400°C for 2 h), (c) JT11 (400°C for 3 h), (d) JT12 (400°C for 4 h) at a constant heating rate of 50°C/min. A, anatase; C, carbon.

DMF. The exothermic peaks between 172 and 300ºC may be linked to the pyrolysis of the PAN or to the oxidation reaction of $TiCl_4$ to TiO_2, respectively [29]. The TGA-DSC results are in good agreement with the XRD results shown in Fig. 5. Of note is the lack of any further exothermic peaks and the very gradual or slight weight loss between 400 and 600ºC in the DSC-TGA curves. While this result suggests the complete decomposition of the carbon precursor such as PAN or the volatilization of the residual carbon, there were no phase changes from anatase to either rutile or brookite. Instead, the heat-treatment process enhanced the oxidation of $TiCl_4$ and the formation of the pure anatase TiO_2 phase, which was relatively thermally stable. No phase evolution or transformation occurred in the as-synthesized TiO_2 nanocrystals despite the increase in the pyrolysis temperature. However, the stability and formation of a specific polymorph of TiO_2 depends on surface free energy, surface stress and most importantly on the particle size [30]. Li et al. [31] previously reported that the anatase polymorph of TiO_2 with a particle size less than 14 nm was more thermodynamically stable than that of the rutile or brookite. Abdo et al. [21] reported an exothermic reaction for typical PAN/Ag particles in a temperature range from 200 to 350ºC. The authors ascribed the exothermic peaks at 300ºC to the cyclization of the nitrile groups of the PAN and to the loss of HCN, N_2 and others. This also agrees with the studies by Miao et al. [30] and Suwarnkar et al. [32] who independently linked the exothermic peaks localised in this temperature range to the degradation of organic residues or moieties.

3.1.4. XRD analysis of the supported TiO_2 nanocrystals

XRD was used for phase identification and estimation of the average crystallite sizes of the synthesized supported catalysts at 300, 350, and 400ºC for different holding times of 1–4 h in a N_2 atmosphere at 20 mL/min as previously noted. The results of the XRD analysis of the supported TiO_2 nanocrystals pyrolyzed in the furnace at different temperatures and holding times are shown in Figs. 5-7.

Figs. 5-7 show the XRD patterns of the supported catalysts All the XRD patterns except for those in Fig. 6a-c clearly show strong, sharp and relatively intense diffraction peaks at 2 θ values of 25.3º, 37.8º, 49.55º, 55.10º, 62.60º, 68.8º, and 75.70º irrespective of the holding time. These diffraction peaks indicate the presence of anatase TiO_2 with the crystal planes (101), (004), (200), (211), (204), (220), and (215). For each holding time, the XRD patterns showed the formation of the pure anatase polymorph of TiO_2 (JCPDS: No 21-1272). There were no rutile or brookite phases detected within the X-ray detection limit at each holding time. In contrast, the XRD pattern for 300ºC and a 1 h holding time (Fig. 6a) had additional weak diffraction peaks at

26.3º, 36.1º, 39.2º 41.8º, 45.4º, and 60.5º, which correspond to the crystal planes (002), (111), (100), (200), (204), and (220) for a typical carbon species originating from PAN. At this holding time and temperature, it was shown that the pyrolysis of PAN and the oxidation of the $TiCl_4$ precursor into TiO_2 occurred concurrently. On the other hand, at 300ºC for 1 h, the diffraction peaks at 72.4º, which correspond to the crystal plane (220) in anatase TiO_2, had yet to develop, which suggests the slow growth of the TiO_2 crystallites. Furthermore, as shown in Fig. 6a-c, the diffraction peak intensity at 36.1º for the crystal plane (111) decreased significantly with an increase in the holding time from 1 to 3 h. This could be due to further decomposition of the PAN. Moreover, as the holding time increased from 2 to 3 h at 300ºC, the diffraction peak of (220) became more intense indicating crystal growth while several other carbon peaks that had been identified at the 1 h holding time disappeared. The intensity of the diffraction peak at (220) increased up to the 4 h holding time. Furthermore, after the 3 h holding time, the peak corresponding to the carbon crystal plane (111) disappeared completely. This result suggests the pyrolysis of the graphitic species derived from the PAN [33]. Despite the broad diffraction peaks and the presence of carbon species, the synthesized supported TiO_2 nanocrystals were still dominated by a pure anatase crystallite phase. This result is in agreement with Shirke et al. [25] who also obtained a pure anatase phase for unsupported TiO_2 nanoparticles synthesized by a microwave assisted sol-gel method calcined at 300ºC for 1 h. Conversely, Li et al. [14] did not obtain peaks corresponding to an anatase phase for TiO_2 nanoparticles annealed at 300ºC for 1 h. Instead, they found that a mixture of rutile and brookite phases dominated. Leong et al. [29] previously reported that during the thermal treatment of a sol-gel solution containing a titanium precursor at different calcination temperatures, the Ti-O-Ti bonds in the sol-gel crystallize into TiO_2, and the heat results in residual water loss and the loss of other volatile organic components. Thus, the complete morphological transformation observed by HRSEM (Figs. 1-3) at 350 and 400ºC irrespective of the holding time suggests that all the $TiCl_4$ precursor species were converted to form TiO_2. Furthermore, the XRD patterns of the supported catalyst annealed at 350 and 400ºC (Figs. 5 and 7) for different holding times are similar. It should be noted that the peak at 26.3º, attributed to carbon species, was common to all samples especially at 350 and 400ºC. This suggests the existence of a Ti-O-C bond and the substitutional effect of Ti in TiO_2 by a carbon species from the PAN precursor. This result corroborates the XPS results shown in Fig. 8. The pyrolyzed samples at 350–400ºC had a pure anatase crystalline phase shown in the XRD patterns (Figs. 5-7) for which the peak intensity increased monotonically with the holding time, and the full width at half maximum of the peaks became narrower. A sharp and more intense diffraction peak observed at different holding times was attributed to the heat treatments which increase the crystallinity and average crystallite size. This is, however, different to the broad diffractograms observed at 300ºC shown in Fig. 6. Critical evaluation of the relative intensity of the characteristic diffraction peaks (Figs. 5-7) for all the synthesized catalysts indicated that the TiO_2 crystallization process was promoted by both the pyrolysis temperature and holding time (see Table 2). The average crystallite size was calculated using the reflection (101) and the Debye-Scherrer equation shown in Eq. 3.

$$d = \frac{k\lambda}{\beta\cos\theta} \quad (3)$$

Here, d is the crystallite size in nanometers; K=0.94; λ is the wavelength of the X-ray which is 0.1541 nm; θ is the half-diffraction angle, and β is the full width at half-maximum in radians for the 2 θ value (25.30). Using the above equation, the average crystalline size for each applied condition was estimated, and the obtained values are shown in Table 3. The 2 θ value (25.30º), θ (12.65º) and cos θ (0.9757) at 300, 350, or 400ºC were the same irrespective of the holding time.

Table 3 shows that as the pyrolysis time were increased for each temperature, the crystals became larger. Additionally, as the temperature was increased, the crystal size increased. The average particle size increased as the holding time was increased especially for samples JT5-JT8 and JT9-JT12 (Table 3). This suggests that the particle size and crystalline phase depend on the pyrolysis temperature as well as the holding time. By comparing the particle size of the various synthesized TiO_2 nanocrystals at different temperatures and holding times, Table 3 clearly shows that the particle size of the supported TiO_2 nanocrystals pyrolyzed at 300ºC (Fig. 6) for 1–4 h increased from 5.01 to 7.09 nm as the holding time was increased. The small nanoparticle size was shown by peak broadening caused by the growth/nucleation of the TiO_2 crystals during extended heating. Thus, the thermal treatment of 8% PAN/DMF/$TiCl_4$ in a N_2 atmosphere at different temperatures and holding times had a significant impact on the nature of the TiO_2 and determined the average crystallite sizes [34]. This study further demonstrated a way to control the particle size of TiO_2 directly in one step during the supporting procedures. Luo et al. [26] previously reported a similar behavior for

Table 2. Crystallite size of the synthesized supported TiO_2 pyrolyzed at 300, 350, and 400ºC for holding times of 1-4 h

Sample	Width in half-high/º	Width/radian	Particle size (nm, XRD)
300ºC			
JT1	1.70	0.0296	4.05
JT2	1.90	0.0333	5.01
JT3	1.30	0.0227	6.51
JT4	1.20	0.0209	7.09
350ºC			
JT5	0.81	0.0140	10.6
JT6	0.75	0.0130	11.4
JT7	0.66	0.0114	13.0
JT8	0.65	0.0114	13.3
400ºC			
JT9	1.1	0.0191	11.2
JT10	0.80	0.0139	13.6
JT11	0.75	0.0131	14.2
JT12	0.60	0.0104	14.3

XRD, X-ray diffraction.

PAN/TiO_2 nanoparticles synthesized from a pre-oxidized PAN/DMF solution containing titanium precursor in normal air. Gupta et al. [35] showed that the calcination of unsupported TiO_2 powder in air at 450ºC for 30 min increased both the crystallinity and its photocatalytic activity. Their results, however, contradict the findings of Dong et al. [36] who reported that thermal treatment of unsupported TiO_2 nanoparticles prepared from a mixture of $Ti(SO_4)_2$, $C_{12}H_{22}O_{11}$ and H_2O followed by calcination at 100, 200, and 300ºC for 2 h had no effect on the average crystal size of the TiO_2 nanoparticles.

3.1.5. XPS analysis of the supported TiO_2 nanocrystals

XPS measurements were done to determine the chemical state of each element contained in the supported catalyst synthesized with the sol-gel method. Sample JT7 (prepared at 350ºC for 3 h) was selected for XPS due to its higher surface area and photocatalytic activity compared to the others. The photocatalytic activity of the synthesized supported catalysts will be provided in a subsequent publication. Fig. 8 shows a XPS survey of the supported TiO_2 nanocrystals pyrolyzed at 350ºC for 3 h, which indicates the presence of Ti, O, C, Fe, Cl, and N. Figs. 9 and 10 show high resolution XPS scans of the individual elements Ti 2p, O 1s and C 1s.

The binding energy peak position of Ti $2p_{3/2}$ at 458.8 eV as well as the difference between the Ti $2p_{3/2}$ and the Ti $2p_{1/2}$ spin orbit splitting of 5.5 eV (see Fig. 9a) clearly indicates that the Ti is in a Ti^{4+} state. Because XPS is a surface sensitive technique and Ti^{3+} on the surface is unstable in air and easily oxidized, one would not expect Ti^{3+} under these conditions. According to the literature, the chemical state of Ti reported in XPS studies for typical pure anatase TiO_2 nanoparticles is Ti^{4+}. The obtained binding energies for Ti and O corroborated the XPS data reported in the literature for typical TiO_2 nanoparticles [37-39]. In the high resolution XPS spectrum of O 1s (Fig. 9b), the peaks fitted at 530.6, 531.7 and 532.9 eV relate to the Ti-O, O-C, and C=O bonds, respectively.

To determine the states of the carbon in the supported TiO_2 nanocrystals (JT7), the C 1s shell was measured, and the scanned results are shown in Fig. 10. Three prominent peaks, which correspond to C-C or C=C, C-O and C=O or COO bonds, were observed in the binding energy region. The presence of elemental carbon could be attributed to the pyrolysis of the polymer precursor (PAN) to carbon. The doping effect of carbon on the supported TiO_2 nanocrystals further corroborated the EDS and XRD results shown in Table 3 and Fig. 5, respectively. There is no noticeable peak for the Ti-C bond in the binding region of 281.0 eV, which suggests no Ti-C bonds exist in the synthesized supported material. Studies have shown that the carbonization

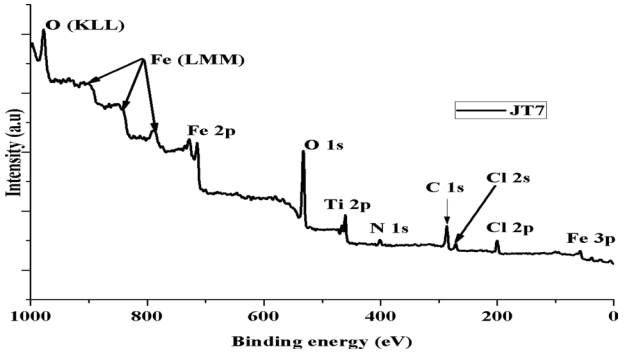

Fig. 8. An X-ray photoelectron spectroscopy survey of sample JT7 showing the elements within the detection limit of the spectrometer

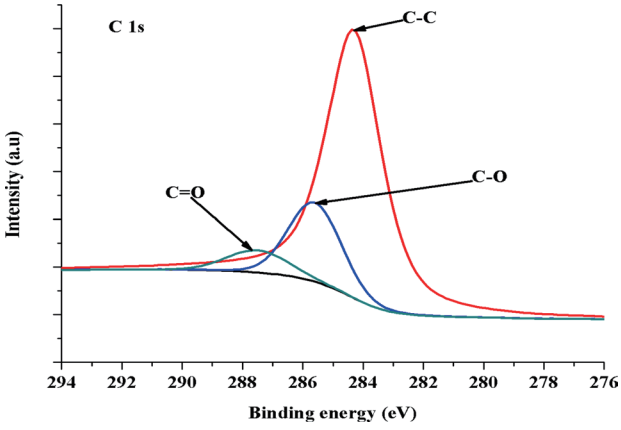

Fig. 10. High resolution-X-ray photoelectron spectroscopy scan of the C 1s binding energy enveloped in sample JT7

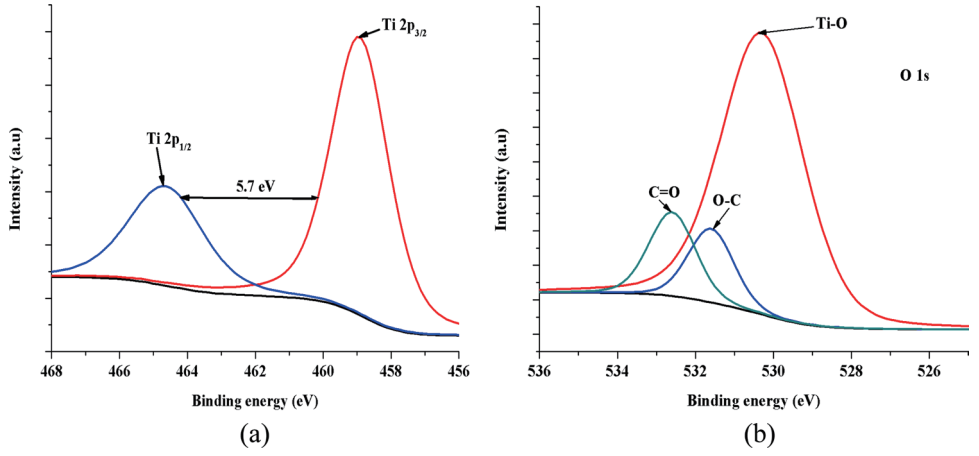

Fig. 9. (a) A detail X-ray photoelectron spectroscopy (XPS) scan of the Ti 2p energy, (b) the XPS spectrum of the O 1s energy enveloped in JT7

process of PAN contributed about 90% of the carbon to the synthesized Ag/PAN nanoparticles [21]. Ren et al. [40] ascribed the two peaks observed at 284.8 and 288.6 eV to the formation of carbon-doped TiO_2 nanoparticles. Nevertheless, comparatively, the combined XPS spectra of Ti 2p, O 1s and C 1s indicated the formation of Ti-O-C due to the pyrolysis of the PAN and the transformation of $TiCl_4$ during the heating process. Furthermore, the presence of C-C, C-O and C=O or COO bonds in the TiO_2 crystals indicates that the carbon was doped onto the TiO_2 nanoparticles. The doping effect of the carbon species on the TiO_2 nanocrystals by PAN might be responsible for the smaller particle size (see the XRD results in Fig. 5). Cong et al. [41] reported similar observations during the synthesis of carbon doped TiO_2 coated on multi-walled carbon nanotubes. The authors ascribed the formation of the Ti-O-C bonds to the close interaction between the TiO_2 lattice structure and the multi-walled carbon nanotubes. In contrast, Rodríguez-González et al. [39] linked the formation of the Ti-O-C bonds to the substitution effect of the carbon atoms on the lattice titanium atoms and not on the oxygen atoms. In addition, the presence of impurities or contamination such as Fe in the XPS survey (Fig. 8) could be due to the heating of the stainless steel mesh, which may have caused the diffusion of atoms, mostly Fe, into the TiO_2 lattice structure. The presence of other elements such as Cl and N are possibly the remnants of the titania and polymer precursors. Luo et al. [26] ascribed the elements C and N that were detected in the XPS spectra to the PAN molecules, respectively. Fernández et al. [13] previously reported the presence of Fe^{3+}, Cr^{3+}, and Si^{4+} in TiO_2 nanoparticles developed on stainless steel with an electrophoretic deposition method. The supported TiO_2 nanoparticles were pyrolyzed in a N_2 atmosphere at 700ºC for 30 min, and the authors attributed the existence of these heterocations to the thermal treatment which promoted the diffusion of some ions (Fe^{3+}, Cr^{3+} and Si^{4+}) from the stainless steel into the TiO_2 layer.

3.1.6. BET surface area of the as-synthesized supported TiO_2 nanocrystals

The textural properties of the as-synthesized supported TiO_2 nanocrystals were investigated using a Micrometrics ASAP 2020 surface area and Porosity Analyzer. The N_2 adsorption–desorption isotherms of the supported TiO_2 nanocrystals pyrolyzed at 300ºC, 350ºC, and 400ºC for 3 h (JT3, JT7, JT11) are shown in Fig. 11. The BET surface areas and the pore areas as determined by the BET and Barrett-Joyner-Halenda methods are listed in Table 3.

According to the International Union of Pure and Applied Chemistry (IUPAC) nomenclature, the adsorption-desorption branches of the JT3, JT7 and JT11 specimens (Fig. 11) can be categorized as a typical type IV isotherm, which belongs to a hysteresis loop type III indicating a purely mesoporous material with small pore sizes. Adsorption type IV indicates capillary condensation of gases within the mesopores as the relative pressure (P/Po) approaches unity. The hysteresis loop consists of both sloping adsorption and a moderately sharp desorption branch even in a high relative pressure (P/Po) range. Table 2 shows that JT7 has the highest BET surface area and micropore area at 152 m^2/g and 35.3 m^2/g, respectively. The formation of the micropore surface area could be due to the intercrystalline voids formed during the agglomeration of the TiO_2 nanocrystals evident in the HRSEM images (Figs. 1-3). The overall BET surface area could be due to the formation of larger mesopores which would reduce surface area during the pyrolysis process because the volatile components from the PAN degradation evaporated during the heat treatment. As seen in Table 2, the particle size increased with an increase in the pyrolysis temperature and holding time although the BET surface area of these samples did not follow a similar trend. The obtained BET surface areas for all the samples are however much higher than the 56 m^2/g reported for the commercial TiO_2 nanoparticles [27,42]. The increased specific surface area could be attributed to the pyrolysis temperature and possibly the doping effect of the carbon from the PAN. The supported TiO_2 nanocrystals pyrolyzed at 350ºC for 3 h (JT7) had a higher surface area compared to the samples prepared at the other temperatures. It was evident that at 300ºC for 3 h (JT3), the PAN was still partially stable because most nanocrystals were still embedded in the polymer shown by the HRSEM results in Fig. 2. At 300ºC, the adsorption-desorption isotherms are nearly flat with the hysteresis loops becoming smaller as the relative pressure approached unity. With an increase in the temperature to 350ºC, extensive pyrolysis of the bulk PAN occurred, and a high mesoporosity was observed due to the formation

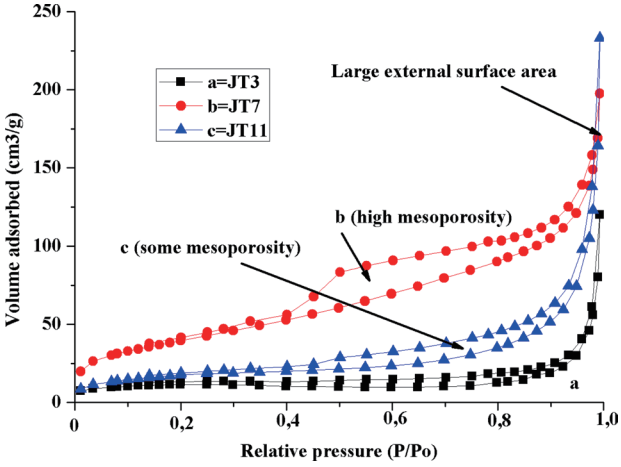

Fig. 11. N_2 adsorption-desorption isotherm plots of (a) JT3 (300ºC for 3 h), (b) JT7 (350ºC for 3 h), and (c) JT11 (400ºC for 3 h).

Table 3. Specific surface area and micropore area of the supported as-synthesized carbon doped TiO_2 nanocrystals compared to the commercial powder Degussa P25

Sample	BET surface area (m^2/g)	Micropore area (m^2/g)
P25 (commercial TiO_2)	56	18
JT3 (300ºC for 3 h)	107	24
JT7 (350ºC for 3 h)	152	35
JT11 (400ºC for 3 h)	132	31

of gaseous species during the volatilization of the PAN, and fully grown TiO_2 crystallites were observed. Further increasing the pyrolysis temperature to 400ºC led to a reduction in the BET surface area and a lower mesoporosity. A study done by Chen et al. [43] reported a decrease in the specific surface area and pore volumes of TiO_2 nanoparticles as the calcination temperatures were increased from 400 to 500ºC, in which the reduction was attributed to uncontrollable destruction of the porous structure. In addition, Leong et al. [29] and Sheikhnejad-Bishe et al. [42] independently ascribed the decline in the surface area to the gradual increase in particle size during calcination.

4. Conclusions

In summary, this study showed that carbon doped TiO_2 nanocrystals can easily be supported on a stainless steel mesh and adhere well forming a robust composite. It was found that carbonaceous species derived from the PAN during the pyrolysis process had a role in the formation and adhesion of the TiO_2 nanocrystals and did not only bond the TiO_2 nanocrystals onto the stainless steel but equally acted as a carbon doping source of the TiO_2 layers. This means that the synthesized TiO_2 photocatalyst was actually carbon doped TiO_2 nanocomposites and that PAN can simultaneously serve as a carbon dopant and stabilizing agent. PAN pyrolysis, instead of calcination, enables controlling the carbon content, and the mesoporosity can be tailored by the temperature. It is possible to conclude that supported TiO_2 nanocrystals prepared by pyrolysis at 300, 350, and 400ºC for 3 h were actually supported carbon doped TiO_2 nanocrystals and that PAN/DMF/$TiCl_4$ offers a facile sol-gel related route for preparing supported carbon doped TiO_2 nanocomposites in one step. This study further showed a way to control the particle size of TiO_2 directly in one step during supporting procedures. Among all the samples, the product obtained at 350ºC (3 h) was the most robust composite with optimum carbon doping and porosity. This study showed how applying the thermal profile enables the controlled tailoring of the composite supported carbon doped TiO_2. Future work will investigate the photocatalytic activity and the diffusion adhesion between the stainless steel and the TiO_2 particles. Additionally, a surface segregation study involving the qualitative behavior of the surface of the steel as a function of the temperature will be done.

Conflict of Interest

No potential conflict of interest relevant to this article was reported.

Acknowledgements

The authors acknowledge the Water Research Commission, South Africa (WRC Project number: K5/2364) for funding the research and the Environmental and Nano Sciences Group, Department of Chemistry, University of the Western Cape for assistance.

References

[1] Ahmed S, Rasul MG, Brown R, Hashib MA. Influence of parameters on the heterogeneous photocatalytic degradation of pesticides and phenolic contaminants in wastewater: a short review. J Environ Manage, **92**, 311 (2011). https://doi.org/10.1016/j.jenvman.2010.08.028.

[2] Hintsho N, Petrik L, Nechaev A, Titinchi S, Ndungu P. Photocatalytic activity of titanium dioxide carbon nanotube nano-composites modified with silver and palladium nanoparticles. Appl Catal B Environ, **156-157**, 273 (2014). https://doi.org/10.1016/j.apcatb.2014.03.021.

[3] Dolat D, Quici N, Kusiak-Nejman E, Morawski AW, Puma GL. One-step, hydrothermal synthesis of nitrogen, carbon co-doped titanium dioxide (N,C– TiO_2) photocatalysts: effect of alcohol degree and chain length as carbon dopant precursors on photocatalytic activity and catalyst deactivation. Appl Catal B Environ, **115-116**, 81 (2012). https://doi.org/10.1016/j.apcatb.2011.12.007.

[4] Lee JH, Kim IK, Cho D, Youn JI, Kim YJ, Oh HJ. Photocatalytic performance of graphene/Ag/TiO_2 hybrid nanocomposites. Carbon Lett, **16,** 247 (2015). https://doi.org/10.5714/CL.2015.16.4.247.

[5] Malato S, Fernández-Ibáñez P, Maldonado MI, Blanco J, Gernjak W. Decontamination and disinfection of water by solar photocatalysis: recent overview and trends. Catal Today, **147**, 1 (2009). https://doi.org/10.1016/j.cattod.2009.06.018.

[6] Saud PS, Ghouri ZK, Pant B, An T, Lee JH, Park M, Kim HY. Photocatalytic degradation and antibacterial investigation of nano synthesized Ag_3VO_4 particles @PAN nanofibers. Carbon Lett, **18**, 30 (2016). https://doi.org/10.5714/CL.2016.18.030.

[7] El-Kalliny AS, Ahmed SF, Rietveld LC, Appel PW. Immobilized photocatalyst on stainless steel woven meshes assuring efficient light distribution in a solar reactor. Drinking Water Eng Sci, **7**, 41 (2014). https://doi.org/10.5194/dwes-7-41-2014.

[8] Friedmann D, Mendive C, Bahnemann D. TiO_2 for water treatment: parameters affecting the kinetics and mechanisms of photocatalysis. Appl Catal B Environ, **99,** 398 (2010). https://doi.org/10.1016/j.apcatb.2010.05.014.

[9] Monreal HA, Chacon-Nava JG, Arce-Colunga U, Martinez CA, Casillas PG, Martınez-Villafane A. Sol–gel preparation of titanium dioxide nanoparticles in presence of a linear polysaccharide. Micro Nano Lett, **4**, 187 (2009). https://doi.org/10.1049/mnl.2009.0070.

[10] Bestetti M, Sacco D, Brunella MF, Franz S, Amadelli R, Samiolo L. Photocatalytic degradation activity of titanium dioxide sol–gel coatings on stainless steel wire meshes. Mater Chem Phys, **124**, 1225 (2010). https://doi.org/10.1016/j.matchemphys.2010.08.062.

[11] Wang C, Li Y, Shi H, Huang J. Preparation and characterization of natural zeolite supported nano TiO_2 photocatalysts by a modified electrostatic self-assembly method. Surf Interface Anal, **47**, 142 (2015). https://doi.org/10.1002/sia.5686.

[12] Zhang TH, Piao LY, Zhao SL, Xu Z, Wu Q, Kong C. Application of TiO_2 with different structures in solar cells. Chin Phys B, **21**, 118401 (2012). https://doi.org/10.1088/1674-1056/21/11/118401.

[13] Fernández A, Lassaletta G, Jiménez VM, Justo A, González-Elipe AR, Herrmann JM, Tahiri H, Ait-Ichou Y. Preparation and characterization of TiO_2 photocatalysts supported on various rigid supports (glass, quartz and stainless steel): comparative studies of photocatalytic activity in water purification. Appl Catal B Environ, **7**, 49 (1995). https://doi.org/10.1016/0926-3373(95)00026-7.

[14] Li W, Shah IS, Sung M, Huang CP. Structure and size distribution of TiO2 nanoparticles deposited on stainless steel mesh. J Vac Sci Technol B Nanotechnol Microelectron Mater Process Meas Phenom, **20**, 2303 (2002). https://doi.org/10.1116/1.1520557.

[15] Zhang L, Zhu Y, He Y, Li W, Sun H. Preparation and performances of mesoporous TiO_2 film photocatalyst supported on stainless steel. Appl Catal B Environ, **40**, 287 (2003). https://doi.org/10.1016/S0926-3373(02)00154-6.

[16] Habibi S, Fatemi S, Izadyar S, Mousavand T. TiO_2 nanoparticle layer formation on ceramic support, a statistical approach to control influential synthesis parameters. Powder Technol, **229**, 51 (2012). https://doi.org/10.1016/j.powtec.2012.06.004.

[17] Wang C, Shi H, Li Y. Synthesis and characterization of natural zeolite supported Cr-doped TiO_2 photocatalysts. Appl Surf Sci, **258**, 4328 (2012). https://doi.org/10.1016/j.apsusc.2011.12.108.

[18] Omri A, Benzina M, Bennour F. Industrial application of photocatalysts prepared by hydrothermal and sol–gel methods. J Ind Eng Chem, **21**, 356 (2015). https://doi.org/10.1016/j.jiec.2014.02.045.

[19] Rahaman MSA, Ismail AF, Mustafa A. A review of heat treatment on polyacrylonitrile fiber. Polym Degrad Stab, **92**, 1421 (2007). https://doi.org/10.1016/j.polymdegradstab.2007.03.023.

[20] Lee HM, Kim HG, An KH, Kim BJ. Effects of pore structures on electrochemical behaviors of polyacrylonitrile-based activated carbon nanofibers by carbon dioxide activation. Carbon Lett, **15**, 71 (2014). https://doi.org/10.5714/CL.2014.15.1.071.

[21] Abdo HS, Khalil KA, Al-Deyab SS, Altaleb H, Sherif ESM. Antibacterial effect of carbon nanofibers containing Ag nanoparticles. Fibers Polym, **14**, 1985 (2013). https://doi.org/10.1007/s12221-013-1985-3.

[22] Ba-Abbad MM, Kadhum AAH, Mohamed AB, Takriff MS, Sopian K. Synthesis and catalytic activity of TiO_2 nanoparticles for photochemical oxidation of concentrated chlorophenols under direct solar radiation. Int J Electrochem Sci, **7**, 4871 (2012).

[23] Chang JA, Vithal M, Baek IC, Seok SI. Morphological and phase evolution of TiO_2 nanocrystals prepared from peroxotitanate complex aqueous solution: Influence of acetic acid. J Solid State Chem, **182**, 749 (2009). https://doi.org/10.1016/j.jssc.2008.12.024.

[24] Cao T, Li Y, Wang C, Shao C, Liu Y. One-step nonaqueous synthesis of pure phase TiO_2 nanocrystals from $TiCl_4$ in butanol and their photocatalytic properties. J Nanomater, **2011**, 267415 (2011). https://doi.org/10.1155/2011/267415.

[25] Shirke BS, Korake PV, Hankare PP, Bamane SR, Garadkar KM. Synthesis and characterization of pure anatase TiO_2 nanoparticles. J Mater Sci Mater Electron, **22,** 821 (2011). https://doi.org/10.1007/s10854-010-0218-4.

[26] Luo Q, Li X, Li X, Wang D, An J, Li X. Visible light photocatalytic activity of TiO_2 nanoparticles modified by pre-oxidized polyacrylonitrile. Catal Commun, **26**, 239 (2012). https://doi.org/10.1016/j.catcom.2012.06.008.

[27] Janus M, Tryba B, Kusiak E, Tsumura T, Toyoda M, Inagaki M, Morawski AW. TiO_2 nanoparticles with high photocatalytic activity under visible light. Catal Lett, **128**, 36 (2009). https://doi.org/10.1007/s10562-008-9721-0.

[28] Shin HK, Park M, Kim HY, Park SJ. An overview of new oxidation methods for polyacrylonitrile-based carbon fibers. Carbon Lett, **16**, 11 (2015). https://doi.org/10.5714/CL.2015.16.1.011.

[29] Leong KH, Monash P, Ibrahim S, Saravanan P. Solar photocatalytic activity of anatase TiO_2 nanocrystals synthesized by non-hydrolitic sol-gel method. Sol Energy, **101**, 321 (2014). https://doi.org/10.1016/j.solener.2014.01.006.

[30] Miao G, Chen L, Qi Z. Facile synthesis and active photocatalysis of mesoporous and microporous TiO_2 nanoparticles. Eur J Inorg Chem, **2012**, 5864 (2012). https://doi.org/10.1002/ejic.201200833.

[31] Li Y, Zhang S, Yu Q, Yin W. The effects of activated carbon supports on the structure and properties of TiO_2 nanoparticles prepared by a sol-gel method. Appl Surf Sci, **253**, 9254 (2007). https://doi.org/10.1016/j.apsusc.2007.05.057.

[32] Suwarnkar MB, Dhabbe RS, Kadam AN, Garadkar KM. Enhanced photocatalytic activity of Ag doped TiO_2 nanoparticles synthesized by a microwave assisted method. Ceram Int, **40**, 5489 (2014). https://doi.org/10.1016/j.ceramint.2013.10.137.

[33] Zhang Y, Xu H, Xin Q. Enhanced phenol degradation by pulsed plasma cooperated with TiO2 nanotubes film. Proceeding of 2012 Asia Pacific Conference on Environmental Science and Technology, Kuala Lumpur, 376 (2012).

[34] Xie Y, Heo SH, Yoo SH, Ali G, Cho SO. Synthesis and photocatalytic activity of anatase TiO_2 nanoparticles-coated carbon nanotubes. Nanoscale Res Lett, **5**, 603 (2009). https://doi.org/10.1007/s11671-009-9513-5.

[35] Gupta K, Singh RP, Pandey A, Pandey A. Photocatalytic antibacterial performance of TiO_2 and Ag-doped TiO_2 against S. aureus. P. aeruginosa and E. coli. Beilstein J Nanotechnol, **4**, 345 (2013). https://doi.org/10.3762/bjnano.4.40.

[36] Dong F, Guo S, Wang H, Li X, Wu Z. Enhancement of the visible light photocatalytic activity of C-doped TiO_2 nanomaterials prepared by a green synthetic approach. J Phys Chem C, **115**, 13285 (2011). https://doi.org/10.1021/jp111916q.

[37] Aziz AA, Puma GL, Ibrahim S, Saravan P. Preparation, characterisation and solar photoactivity of titania supported strontium ferrite nanocomposite photocatalyst. J Exp Nanosci, **8**, 295 (2013). https://doi.org/10.1080/17458080.2012.675087.

[38] Dhabbe RS, Kadam AN, Suwarnkar MB, Kokate MR, Garadkar KM. Enhancement in the photocatalytic activity of Ag loaded N-doped TiO_2 nanocomposite under sunlight. J Mater Sci Mater Electron, **25**, 3179 (2014). https://doi.org/10.1007/s10854-014-2001-4.

[39] Rodríguez-González V, Alfaro SO, Torres-Martínez LM, Cho SH, Lee SW. Silver–TiO_2 nanocomposites: synthesis and harmful algae bloom UV-photoelimination. Appl Catal B Environ, **98**, 229 (2010). https://doi.org/10.1016/j.apcatb.2010.06.001.

[40] Ren W, Ai Z, Jia F, Zhang L, Fan X, Zou Z. Low temperature preparation and visible light photocatalytic activity of mesoporous carbon-doped crystalline TiO_2 Appl Catal B Environ, **69**, 138 (2007). https://doi.org/10.1016/j.apcatb.2006.06.015.

[41] Cong Y, Li X, Qin Y, Dong Z, Yuan G, Cui Z, Lai X. Carbon-doped TiO_2 coating on multiwalled carbon nanotubes with higher visible light photocatalytic activity. Appl Catal B Environ, **107**, 128 (2011). https://doi.org/10.1016/j.apcatb.2011.07.005.

[42] Sheikhnejad-Bishe O, Zhao F, Rajabtabar-Darvishi A, Khodadad E, Mostofizadeh A, Huang Y. Influence of temperature and surfactant on the photocatalytic performance of TiO_2 Nanoparticles. Int J Electrochem Sci, **9**, 4230 (2014).

[43] Chen D, Du G, Zhu Q, Zhou F. Synthesis and characterization of TiO_2 pillared montmorillonites: application for methylene blue degradation. J Colloid Interface Sci, **409**, 151 (2013). https://doi.org/10.1016/j.jcis.2013.07.049.